Spontaneous core-shell elemental distribution in In-rich InxGa1-xN nanowires grown by molecular beam epitaxy

M. Gomez-Gomez, N. Garro, J. Segura-Ruiz, G. Martinez-Criado, A. Cantarero, H. T. Mengistu, A. Garcia-Cristobal, S. Murcia-Mascaros, C. Denker, J. Malindretos, et al.

OPEN ACCESS
IOP Publishing
Nanotechnology

Nanotechnology **25** (2014) 075705 (9pp)
doi:10.1088/0957-4484/25/7/075705

Spontaneous core–shell elemental distribution in In-rich $In_xGa_{1-x}N$ nanowires grown by molecular beam epitaxy

M Gómez-Gómez[1], N Garro[1], J Segura-Ruiz[2], G Martinez-Criado[2], A Cantarero[1], H T Mengistu[1], A García-Cristóbal[1], S Murcia-Mascarós[1], C Denker[3], J Malindretos[3] and A Rizzi[3]

[1] Institut de Ciència dels Materials, Universitat de València, E-46980 Paterna (València), Spain
[2] European Synchrotron Radiation Facility, Experiments Division, F-38043 Grenoble, France
[3] IV Physikalisches Institut, Georg-August-Universität Göttingen, D-37077 Göttingen, Germany

E-mail: nuria.garro@uv.es

Received 2 September 2013
Accepted for publication 11 November 2013
Published 23 January 2014

Abstract

The elemental distribution of self-organized In-rich $In_xGa_{1-x}N$ nanowires grown by plasma-assisted molecular beam epitaxy has been investigated using three different techniques with spatial resolution on the nanoscale. Two-dimensional images and elemental profiles of single nanowires obtained by x-ray fluorescence and energy-dispersive x-ray spectroscopy, respectively, have revealed a radial gradient in the alloy composition of each individual nanowire. The spectral selectivity of resonant Raman scattering has been used to enhance the signal from very small volumes with different elemental composition within single nanowires. The combination of the three techniques has provided sufficient sensitivity and spatial resolution to prove the spontaneous formation of a core–shell nanowire and to quantify the thicknesses and alloy compositions of the core and shell regions. A theoretical model based on continuum elastic theory has been used to estimate the strain fields present in such inhomogeneous nanowires. These results suggest new strategies for achieving high quality non-polar heterostructures.

Keywords: nanowire, alloy, Raman scattering, x-ray fluorescence, EDX

(Some figures may appear in colour only in the online journal)

1. Introduction

Semiconductor nanowires (NWs) based on group-III nitrides have generated much interest in the last decade as they might offer several advantages over bulk and thin layer morphologies. First of all, since NWs have more freedom to relax strain caused by lattice mismatch to the substrate, GaN, InN and AlN NWs free of extended defects have been obtained on silicon, sapphire and other substrates [1–4]. Furthermore, the proximity of the free lateral surface should also enable efficient strain relaxation. This is of paramount importance in the case of $In_xGa_{1-x}N$ ternary alloys, where compositional inhomogeneities and phase segregation hamper the growth of high quality films across the entire range of compositions and thus the tunability of the alloy bandgap from the UV to the IR [5–7]. Last but not least, NW heterostructures can be obtained not only in axial but also in core–shell geometry. Non-polar core–shell NW-based heterostructures should, on the one hand, improve the internal quantum efficiency due to the suppression of the internal electric fields and, on the other hand, disentangle light absorption from radial collection

Table 1. Growth process parameters and characteristic morphology of the $In_xGa_{1-x}N$ NWs investigated: Ga supply (c_{Ga}); substrate temperature (T_s); length (L); and diameter (D). In sample G710 a bimodal distribution with two different average sizes was found and they are labeled A and B.

Sample	c_{Ga} (%)	T_s (°C)	L (nm)	D (nm)
G869	5	458	250–1000	50–500
G682	20	500	500–800	35–60
G692	20	575	450–1100	75–170
G710A	50	550	1200–1300	200–250
G710B	50	550	650–1000	35–65

of photogenerated carriers. Both effects are advantageous for optoelectronic and light-harvesting applications [8].

Molecular beam epitaxy (MBE) could be a suitable technique for growing $In_xGa_{1-x}N$ NWs across the entire compositional range, even for high indium contents, as it allows a relatively low growth temperature as compared to metal organic chemical vapor deposition (MOCVD) for example. This has been pointed out as a key factor for overcoming the alloy miscibility gap [5]. There are a few reports on MBE-grown $In_xGa_{1-x}N$ NWs which show, however, poorer columnar morphology than their binary counterparts [9–11]. Most of the publications to date report on structures where $In_xGa_{1-x}N$ is grown either on top of [12–15] or inserted into GaN NWs [16–20]. Controlling the alloy concentration is also difficult, especially for a high In content. As a consequence, MBE-grown $In_xGa_{1-x}N$ NWs exhibit limited energy tunability and large broadening of their emission peaks, emphasizing the inhomogeneous composition distribution and the strain fields present in these NWs, even in the case of NW insertions [13, 18–20]. Shedding light onto such a complex scenario requires the combination of several characterization techniques with capability of probing single NWs.

In this work we study the elemental distribution of $In_xGa_{1-x}N$ NWs with a high In content grown by MBE. Three techniques are used for the characterization of single NWs. X-ray fluorescence (XRF) imaging carried out with a synchrotron radiation nanoprobe is used for quantitative composition analysis, providing elemental identification with excellent detection limits. Higher spatial resolution is achieved in linear scans of energy-dispersive x-ray spectroscopy (EDX) recorded in a transmission electron microscope (TEM). Finally, Raman scattering provides valuable information about crystalline quality, chemical composition, and strain fields of NW ensembles. When the excitation matches the energy of an electronic transition, resonant Raman scattering (RRS) can be used to study single NWs. Furthermore, RRS offers additional spectral selectivity which allows the study of specific nanometric areas within individual inhomogeneous NWs. For the appropriate interpretation of RRS results, the strain fields in inhomogeneous NWs are calculated with a theoretical model based on continuum elastic theory.

2. Experimental details

In-rich $In_xGa_{1-x}N$ NWs were grown on a rotating n-type Si(111) substrate by catalyst-free plasma-assisted MBE in a

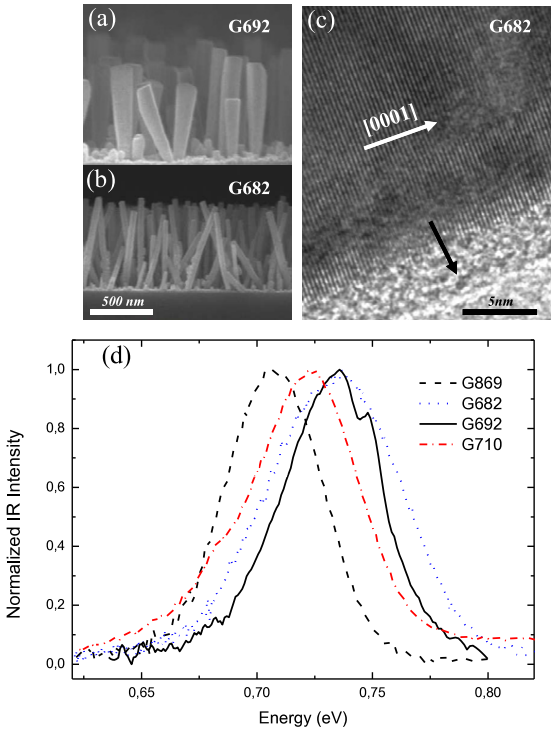

Figure 1. SEM side-view images of as-grown $In_xGa_{1-x}N$ NW ensembles with the same nominal composition and different T_s: sample G692 (a) and sample G682 (b). (c) HRTEM micrograph showing the atomic planes close to the lateral surface of a single $In_xGa_{1-x}N$ NW from G682. The amorphous material at the surface, indicated by an arrow, could be a thin oxide layer. (d) Normalized PL spectra in the IR range of $In_xGa_{1-x}N$ NW ensembles of the investigated samples measured at 10 K.

Veeco Gen-II system. The active nitrogen was supplied by a radio frequency plasma source (UNI-Bulb), whereas standard effusion cells provided In and Ga. Nitrogen-rich conditions were kept during the growth time (of 200 min for all samples). The Ga supply, c_{Ga}, defined as the Ga/(In + Ga) flux ratio and the substrate temperature, T_s, were varied as shown in table 1. T_s was measured with a pyrometer (Ircon modline 3, 32-13C10, $\epsilon = 0.639$).

Dense ensembles of free standing $In_xGa_{1-x}N$ NWs (density ~5–50 NWs μm^{-2}) are obtained by MBE for the three different Ga relative supplies explored in this work. There is a large dispersion in the lengths (L) and diameters (D) of NWs belonging to the same sample and their range, gathered in table 1, is very dependent on T_s, as can be seen in the scanning electron microscopy (SEM) images of figures 1(a) and (b). For the same c_{Ga} but increasing T_s, there is a reduction in the density of the ensemble accompanied by an increase in the NW diameter, especially at the top end of the NW (the wires adopt a baseball bat shape). For the highest c_{Ga}, the size of the NWs falls into a bimodal distribution with two characteristic values for L and D, as reported in table 1. High resolution TEM (HRTEM) images, like that of figure 1(c), show the high structural quality of the grown NWs.

The NW ensembles have been characterized by photoluminescence (PL). The samples were held in a closed cycle He cryostat and excited with several visible and ultraviolet

lines from an Ar laser. The PL signal was dispersed in a 0.18 m monochromator and detected with either a InGaAs photodiode, for the infrared (IR) range of the spectrum, or a charge coupled device (CCD), for the visible and ultraviolet ranges. All samples presented an emission peak in the IR range, as shown in figure 1(d), while only two of them, G682 and G710, showed a second broader PL band in the visible range (not shown). The central energies of the IR PL peaks are close to the bandgap energy of pure InN (0.67 eV) and show no correlation with c_{Ga}.

For the analysis of single NWs, they were scraped off the substrate and dispersed onto a different substrate. Several tens of single NWs were isolated and investigated by three different techniques. For XRF and RRS, gold and aluminum patterned substrates with 50×50 μm^2 grids were used to facilitate the location of single NWs previously imaged by SEM. Commercial holey carbon films supported by standard Cu grids were used for HRTEM–EDX measurements.

The RRS measurements were performed in backscattering geometry using either an Ar/Kr laser or an IR laser diode as the excitation source. The laser light was focused onto a 1 μm-diameter spot by means of a Nikon microscope objective (100×, NA =0.90). The scattered light was analyzed with a Jobin-Yvon T64000 triple spectrometer equipped with a liquid nitrogen cooled CCD detector.

The nanoimaging station ID22NI at the European Synchrotron Radiation Facility hosted the XRF measurements. The x-ray beam was focused by a pair of Kirkpatrick–Baez multilayer coated Si mirrors providing a spot size of 50×50 nm^2 with a flux of about 10^{12} ph s^{-1} at 17 keV ($\Delta E/E \approx 10^{-2}$) [21]. The detection limit was down to 1 ppm for elements heavier than Ca. Rectangular regions containing single NWs were scanned by the x-ray beam with steps of 25 nm. The XRF signal was detected at 15° with respect to the sample surface using an energy dispersive silicon drift detector. The XRF spectra were analyzed using the non-linear least-squares fitting code PyMca [22].

The HRTEM–EDX measurements were carried out in a FEI Tecnai G^2 system with a Schottky field emission electron gun operated at 200 kV. The sample holder was tilted by 30° with respect to the electron beam to optimize the fluorescence detection. Different dwell times were tested in order to find an optimum value (4 s per point) which avoided beam damage while still providing reasonable counting statistics. The spatial resolution is given by the 3 nm diameter of the electron beam. The commercial software of the instrument provided Cliff–Lorimer *k*-factors for quantitative chemical analysis.

3. Results

3.1. Resonant Raman scattering

Raman scattering measurements on ensembles of free standing NWs were performed using different excitation wavelengths. Figure 2(a) shows the RRS spectra of one of the investigated samples (G692) for three different excitation wavelengths. In the backscattering geometry used in the present experiment,

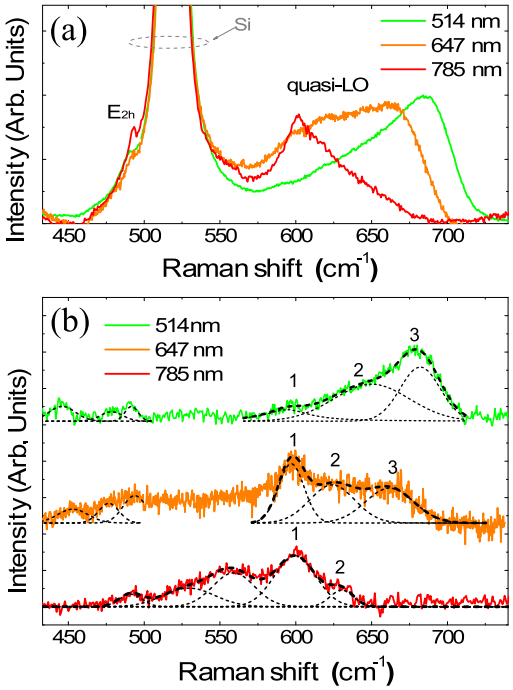

Figure 2. Raman spectra of (a) ensembles and (b) single $In_xGa_{1-x}N$ NWs from sample G692 for excitation wavelengths of 514.5, 647.1, and 785 nm. All measurements were carried out at room temperature in backscattering geometry.

the incident laser beam and the collected scattered light are nearly parallel to the *c*-axis of the NWs of the ensemble. Therefore, there are two phonon modes allowed by the Raman selection rules [23]: E_{2h} [between 488 (InN) and 568 cm^{-1} (GaN) [24]] and A_1(LO) [between 586 (InN) and 734 cm^{-1} (GaN) [24]]. The scattering conditions, however, can deviate from the nominal ones since a significant proportion of the light enters the NWs at a random angle through their lateral surfaces [25]. Then, the A_1(LO) can be mixed with the E_1(LO) mode resulting in a so-called quasi-longitudinal optical (LO) mode at a slightly higher frequency. The E_{2h} peak can be observed in figure 2 as a shoulder on the low energy tail of a very intense peak centered at 520 cm^{-1}, which is coming from the silicon substrate. At higher frequencies, the quasi-LO modes appear in the spectra as broad bands for all the excitation wavelengths, which is a typical sign of inhomogeneities in the alloy composition [27]. Another interesting observation is the shift of the maximum of this band from ∼600 to ∼690 cm^{-1} when the excitation changes from 785 to 514 nm. For higher excitation energies (not shown here) there is no further blue-shift and the quasi-LO band remains like the one obtained for 514 nm. This behavior can be explained by the selective excitation of regions with different Ga contents. The inhomogeneities detected in the NW ensembles could be due either to the existence of NWs with different compositions or to inhomogeneities in the alloy content within single NWs [28].

With the aim of discerning the origin of these inhomogeneities, the RRS spectra of single NWs were measured as a function of the excitation wavelength. In these experiments, the excitation and the scattered light propagate perpendicular to the NW axis, so that the A_1(TO) [between 447 (InN) and

531 cm^{-1} (GaN) [24]] and E_1(TO) modes [between 476 (InN) and 559 cm^{-1} (GaN) [24]] as well as the E_{2h} mode are allowed by Raman selection rules [23]. Three representative spectra are shown in figure 2(b) for different excitation wavelengths. Several weak peaks are resolved at frequencies close to the E_{2h} frequency which could be attributed to transverse optical (TO) modes. At frequencies higher than 586 cm^{-1}, the quasi-LO bands are identified, although these modes are symmetry-forbidden. The occurrence of LO modes has also been reported for InN NWs [26]. The spectral content of the quasi-LO bands is almost identical to those of the NW ensemble, proving that the alloy inhomogeneities come from individual NWs.

The quasi-LO bands can be decomposed into two or three Gaussian peaks depending on the excitation wavelength. The lowest frequency one, labeled 1 in figure 2(b), is centered in a narrow interval (∼594–599 cm^{-1}) and changes significantly with the excitation line. The second spectral contribution of the quasi-LO band, peak 2, becomes more intense and slightly blue-shifts with increasing excitation energy. Both effects are also observed for the third peak, which can only be resolved for red and green excitation lines. Such intensity enhancement is a typical feature of RRS. Since the product of the light penetration and escape depths (estimated as $(2\alpha)^{-1}$) for the excitation energies employed in the current experiments are comparable to the NW diameter [29], the RRS spectra of figure 2(b) are representative of most of the NW volume. Thus, the observed blue-shift of the Raman peaks can be attributed to selective resonant excitation of regions with different Ga content within each single NW.

The frequencies of the LO phonons of $In_xGa_{1-x}N$ shift with the atomic composition following the so-called one-mode-type behavior [27], in which the phonon frequency varies continuously from the mode frequency of one compound to that of the other, as expressed by Vegard's law for A_1(LO): $(1-x) = (\omega - 586)/148$ (with ω being the central frequency of each Gaussian peak in cm^{-1}). It should be pointed out, however, that the phonon frequency is also a sensitive probe of the strain state of nanostructures. Both contributions, alloy composition and strain fields, will be taken into account later in the discussion of the RRS results. On the other hand, the sensitivity of Raman scattering to the disorder inherent in ternary alloys [27] is responsible for the increase in the spectral broadening of the Raman peaks observed in figure 2. This is the main contribution to the uncertainty of the alloy composition deduced by RRS (<15%).

3.2. X-ray fluorescence

The elemental composition of individual NWs has been examined by XRF measurements. The high photon flux of the two-undulator-based nanoprobe provides superior elemental sensitivity in the hard x-ray regime and high spatial resolution capable of resolving single NWs [28, 30]. Figures 3(a) and (b) show the fluorescence intensity maps of the Kα line of Ga and the Lα line of In for a representative single $In_xGa_{1-x}N$ NW from sample G692. The superposition of both elemental intensity maps (see figure 3(c)) shows a higher signal from Ga at the bottom than at the top of the NW (the top and bottom

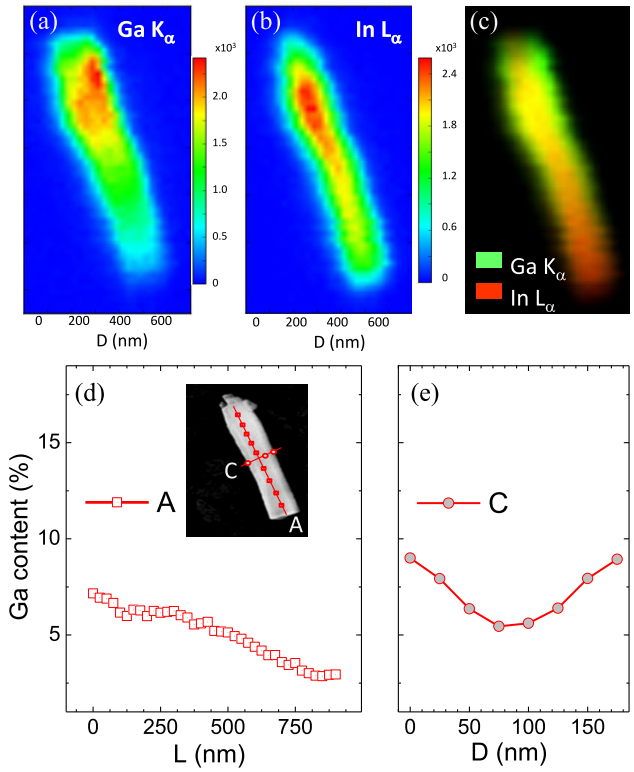

Figure 3. (a) Ga Kα and (b) In Lα fluorescence intensity maps of a $In_xGa_{1-x}N$ single NW from sample G692. The color scale indicates the XRF intensity in photon counts. (c) Superimposed fluorescence intensity maps of In Lα (red) and Ga Kα (green). (d), (e) Ga content along A (the axis of the NW) and C (the center cross-section of the NW), respectively, as depicted in the inset SEM image.

ends of the NW were previously identified in the SEM image of figure 3(d)). Furthermore, there are variations in the relative intensity of In and Ga along the NW radius. The central part, or core, seems to be richer in In than the outer layers, or shell, suggesting the spontaneous formation of a core–shell structure. Although the oversampling of the XRF scan allows a partial definition of the shell region, its thickness cannot be resolved due to the spatial resolution of the technique. Besides the depth resolution, which is determined by the incident x-ray photon energy, the spatial resolution in these XRF measurements is governed by the spot size of the incident beam and the diffusion length of the carriers. Therefore, the resulting spatial resolution should be larger than the spot size.

Quantitative information on the elemental concentration along the NWs can be extracted from the XRF spectra using the relation between the intensity of each elemental fluorescence line, I_i, and its concentration, C_i, which is given by [31]

$$I_i = I_0 k_i C_i \int_0^d e^{-[\mu(h\nu)/\sin\theta_1 + \mu(E_i)/\sin\theta_2]y}\, dy. \qquad (1)$$

For the $In_xGa_{1-x}N$ ternary alloy, Ga and In concentrations are $C_{Ga} = (1-x)$ and $C_{In} = x$. Equation (1) is valid for a flat sample excited by a monochromatic incoming x-ray beam neglecting enhancement effects due to additional excitation of the element of interest by the characteristic radiation of other elements in the sample. I_0 is the intensity of the incoming

beam and k_i accounts for the fluorescence yield, solid angle, and detection efficiency. The attenuation due to the sample thickness, d, is given by the integral, where μ is the total mass absorption coefficient at the energy of the fluorescence, E_i, and the excitation, $h\nu$, and θ_i are the excitation and detection angles relative to the sample surface. As the total mass absorption coefficient of the alloy is given by $\mu = \sum_i C_i \mu_i$, equation (1) has been solved iteratively imposing the stoichiometric condition, $\sum_i C_i = 1$. Special attention has been paid to the variation of the sample thickness along the NW radius. Considering that $\mu d \ll 1$ for our experimental conditions (excitation and detection angles, diameters and alloy compositions) the thin sample approximation has been assumed [31]. Therefore equation (1) has been simplified to

$$I_i \approx I_0 k_i C_i d. \quad (2)$$

Figures 3(d) and (e) show the Ga concentration in different positions along the axis and the diameter at the central height of the studied NW, respectively. The axial line-scan shows that Ga accumulates at the bottom of the NW, whereas the lowest Ga composition is located at the top of the NW. The radial line-scan also shows a gradient in Ga intensity and suggests a higher Ga concentration close to the NW lateral surfaces than in the inner core. The same radial alloy distribution has been observed when the In Kα line was employed for the quantification. The error of these numerical values is of the order of 5% due to the propagation of errors mostly coming from the tabulated parameters of equation (1).

In order to detect any possible radiation damage in the material produced by the x-ray beam, some of the single $In_xGa_{1-x}N$ NWs investigated were characterized by Raman scattering before and after the XRF scans. From the comparison of the Raman spectra we concluded that, at the excitation photon density used in our experiments, the x-ray beam did not inflict measurable changes in the elemental composition and the structural quality of the NWs within the sensitivity of our RRS technique.

3.3. Energy-dispersive x-ray spectroscopy

In order to clarify the spontaneous formation of a core–shell structure in these NWs, HRTEM–EDX measurements were carried out in single NWs, providing higher spatial resolution but worse detection limits than synchrotron-based XRF. HRTEM–EDX offers an improved spatial resolution to the detriment of the signal to noise ratio of the fluorescence intensity. Damage by the electron beam also limits the sensitivity of this technique, as it could cause fluctuations in the In concentration [32].

The HRTEM–EDX intensity profiles obtained in the C radial and axial line-scans of the single NW depicted in figure 4(a) are shown in figures 4(c) and (d), respectively. Each point of the line-scan accounts for the integrated intensity of either the Ga Kα or the In Lα fluorescence lines, as shown in figure 4(b), and is represented as a function of the beam position relative to the NW length and radius. The absolute spatial reference is lost when the single NWs, which are dispersed with random orientation on the holey carbon film, are tilted with respect to the positions of the fluorescence detector. Quantitative values for the alloy composition in the NW were obtained using the Cliff–Lorimer method [33] with the k-factors provided by the commercial software of the instrument. This method relies on the thin sample approximation which, as discussed previously for XRF quantification, can be safely assumed for these NWs. The use of this approximation is also justified by the good correlation (not shown here) between the radial profiles of the HRTEM–EDX intensity of binary GaN and InN single NWs and their corresponding cross-sections. Nevertheless, extra attention is paid to the case of radial line-scans, where the chemical composition changes simultaneously with the sample thickness [34]. Fluorescence spectra measured from two different points in the NW core and shell regions, like those depicted in figure 4(b), show a lower intensity of the In Lα fluorescence line at the shell than at the core, while the intensity of the Ga Kα line remains almost constant. A statistically meaningful number of radial line-scans have been recorded and analyzed for NWs with a random geometrical disposition with respect to the detector. The compositions obtained are consistent and independent of the NW orientation, proving that the existence of a radial gradient of compositions is not an artifact caused by a non-uniform aspect ratio with respect to the detector.

Figure 4(f) shows the radial variation of the Ga content at the center of the NW. The concentration of Ga is approximately constant in the core and then increases continuously towards the lateral surfaces of the NW in the region we have denominated as the shell. The asymmetry observed in this profile could be associated with shadowing effects during the growth. The fact that most of the radial profiles are symmetric rules out other effects related to the HRTEM–EDX collection geometry. The axial line-scan depicted in figure 4(e) shows a non-linear decrease of Ga concentration from the bottom to the top of the NW. The relative uncertainty of the elemental concentrations is now dominated by the counting statistics, as shown in figure 4(b), and reaches a maximum value of 35% in the points closer to the lateral surfaces of the NWs, due to the reduction of the probed volume.

4. Discussion

The three experimental techniques employed in this work are sensitive to alloy compositions but, due to the complexity of the present $In_xGa_{1-x}N$ NWs, which include inhomogeneities at a nanometric length scale, none of them can provide definitive composition values on their own. Thus, the combination of more than one technique, in such a manner that the strengths of one complement the weaknesses of others, is valuable in this case. Both HRTEM–EDX and XRF measurements probe locally the average alloy composition of the excited sample volume, offering complementary spatial resolution and elemental sensitivity, respectively. On the other hand, regions with different alloy composition within the whole NW volume appear as separate peaks in the RRS spectra. The central frequency and the linewidths of these peaks can be interpreted in terms of the alloy composition and the strain fields present in these heterogeneous NWs. Furthermore, their intensities can

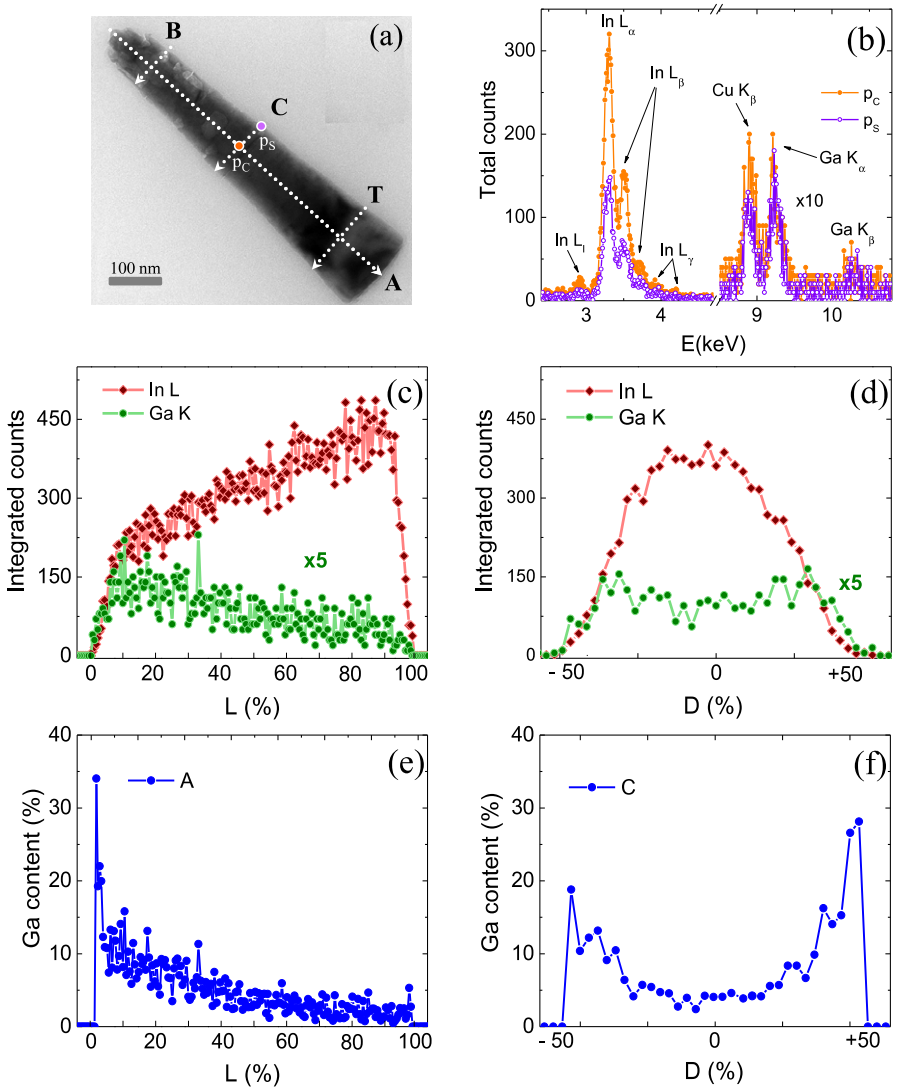

Figure 4. (a) TEM micrograph of a single NW from sample G692. Axial and radial HRTEM–EDX line-scans performed on the NW are depicted and labeled A (axial), B (bottom), C (center) and T (top). (b) Comparison of the fluorescence spectra corresponding to two different points p_C (inner core) and p_S (outer shell). Besides the In L and Ga K fluorescence lines from the NWs, Cu K lines from the TEM grid are also observed. (c), (d) Integrated fluorescence intensity of the Ga Kα and In Lα lines along A and C as depicted in the TEM micrograph, respectively. (e), (f) Ga content deduced from the HRTEM–EDX line-scans along A and C, respectively.

be enhanced when the excitation energy is in resonance with electronic transitions of the NWs.

Let us start by analyzing the HRTEM–EDX and XRF results. Both techniques have evidenced a gradient in the radial alloy distribution with a core–shell structure which should be taken into account in the quantitative interpretation of the experimental profiles. As a first approximation, a cylindrical NW with a sharp transition in the alloy composition between the core and the shell can be assumed. The cross-section of such a model NW is depicted in figure 5(a), where a core of radius R_c and Ga content C_{Ga}^{core}, is surrounded by a shell of thickness t and relative Ga concentration C_{Ga}^{shell}. The shadowed area represents the volume probed by the electron (or x-ray) beam in the HRTEM–EDX (or XRF) line-scan when it is positioned at a distance y from the NW center. In the thin sample approximation, the intensity of the fluorescence lines for each element are proportional to its concentration and to the sample thickness, as shown in equation (2). For EDX line-scans, the finite size of the electron beam can be neglected and each elemental fluorescence line should be given by

$$\begin{aligned} &I_i(y) \propto C_i^{shell}\sqrt{(R_c+t)^2-y^2} \\ &\quad \text{for } R_c+t \geq y > R_c, \\ &I_i(y) \propto C_i^{core}\sqrt{R_c^2-y^2} + C_i^{shell}\left(\sqrt{(R_c+t)^2-y^2}\right. \\ &\left.\quad -\sqrt{R_c^2-y^2}\right) \qquad \text{for } y \leq R_c. \end{aligned} \tag{3}$$

The relative Ga concentration along the diameter of the sharp core–shell NW, calculated as

$$C_{Ga}(y) = \frac{I_{Ga}(y)}{I_{Ga}(y)+I_{In}(y)}, \tag{4}$$

should then be compared with the experimental profiles obtained by HRTEM–EDX. Figure 5(b) displays the best

Table 2. Values for C_{Ga}^{core}, C_{Ga}^{shell}, R_c and t for single representative NWs from sample G692 deduced from the fitting of the HRTEM–EDX and XRF experimental data for cross-sections at the bottom (B), center (C) and top (T) shown in figure 4(a). The slash separates the HRTEM–EDX value (left) from the XRF one (right). Due to the small thickness of the shell, t values are obtained from the fitting of the HRTEM–EDX line-scans only.

Section	C_{Ga}^{core} (%)	C_{Ga}^{shell} (%)	R_c (nm)	t (nm)
B	1/3	41/16–40[a]	40/82	12
C	1/4	32/18	52/74	8
T	1/3	15/9	77/77	5

[a] Values corresponding to the left–right side of the asymmetric XRF profile.

fitting curves for the experimental results for the bottom (B), center (C) and top (T) cross-sections of a representative single NW. A very good agreement is observed for lines C and T, while profile B is less accurate. This could be due to the existence of more than two phases in the bottom part of the NW [35]. Thus the sharp core–shell NW model can be a reasonable first approximation for most of the NW volume, with the exception of the bottom part.

The core and shell Ga contents, R_c, and t obtained from the fittings at the three cross-sections are gathered in table 2. The core of the NWs is almost pure InN, while the shell Ga content exceeds by far the Ga supplied in the growth process at the bottom of the NW and diminishes gradually towards the top. The shell thickness also decreases from bottom to top. The simultaneous reduction of the Ga content and thickness of the shell from the bottom to the top of the NW can explain the slow decrease observed in most of the axial A profile (see figure 5(c)). Again here, the high Ga content found at the base of the NW deviates from the model predictions.

The Ga content obtained by XRF along the different B, C and T cross-sections (see figure 6) can be fitted by the core–shell profile and show equally good agreement. In this case, however, the intensity profiles of equations (3) have been convoluted with a Gaussian of 22.5 nm width in order to account for the 50×50 nm^2 x-ray spot size. Since the size of the x-ray beam makes the fitting of t rather imprecise, this parameter is taken from the HRTEM–EDX results from a different NW. It should be pointed out that the values of t obtained from the HRTEM–EDX analysis of several NWs do not vary substantially with the size of the NW. Table 2 also shows the Ga contents for the core and the shell of a representative NW from sample G692 as obtained from the fitting of its XRF profiles. Concerning the Ga content in these NWs, XRF and HRTEM–EDX results are in remarkably good qualitative agreement. Both techniques corroborate the existence of an almost pure InN core in each NW, which is also in agreement with the IR peak appearing in the PL spectrum of this sample (see figure 1). Furthermore, C_{Ga}^{shell} decreases consistently from the bottom to the top of the NW. The quantification of C_{Ga}^{shell} deviates from one technique to the other and HRTEM–EDX values tend to be overestimated. This last technique presents larger experimental errors, particularly close to the NW shell due to the low count statistics. Nevertheless, the large quantitative

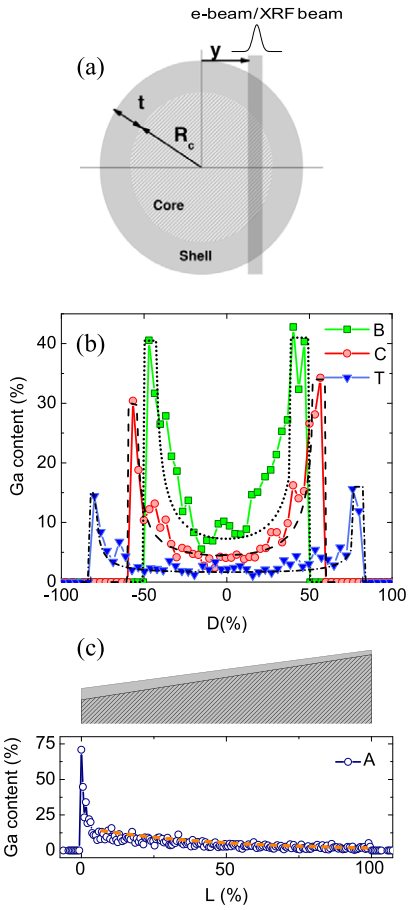

Figure 5. (a) Cross-section of a cylindrical NW with a sharp core–shell structure. An $In_xGa_{1-x}N$ shell of thickness t and Ga content C_{Ga}^{shell} wraps the central core of radius R_c and C_{Ga}^{core}. The shadowed zone represents the area excited by the electron or x-ray beam with a Gaussian intensity profile in HRTEM–EDX and XRF experiments, respectively. (b) Variation of the Ga content deduced from the HRTEM–EDX scans along the B, C and T cross-sectional lines shown in figure 4(a) together with the best fit (dashed lines) obtained assuming a sharp core–shell NW. (c) Variation of the Ga content measured along the A axial line-scan of figure 4(a) and predicted by the sharp core–shell model (dashed line) due to the reduction of t and C_{Ga}^{shell} with height, as shown in the scheme of the longitudinal section.

disagreement observed in the experimental Ga content profiles between figures 5(b) and 6 can be now partly understood as a consequence of the difference between the probed volumes in XRF and HRTEM–EDX experiments and the existence of a shell richer in Ga.

The existence of a core–shell alloy distribution should also be taken into account in the analysis of the RRS experimental results, as this can generate strain fields in the NWs which introduce additional phonon frequency shifts. A survey of HRTEM micrographs of these NWs shows a low density of structural defects in most of the NW volume and, in particular, in the regions close to the NW lateral surface where the transition between the core and the shell should take place. Therefore, it is reasonable to assume that both regions should be lattice matched and, due to the variation of the lattice parameters with alloy composition, strain fields should be

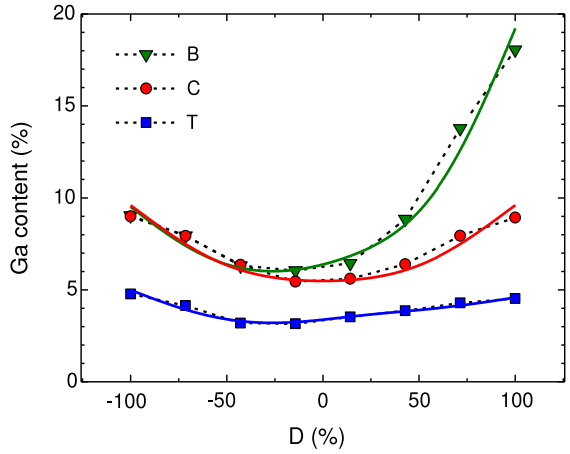

Figure 6. Ga content deduced from the XRF measurements along cross-sections B, C and T. Dotted lines show the theoretical fitting of the experimental data to the sharp core–shell NW model convoluted with a 22.5 nm wide Gaussian.

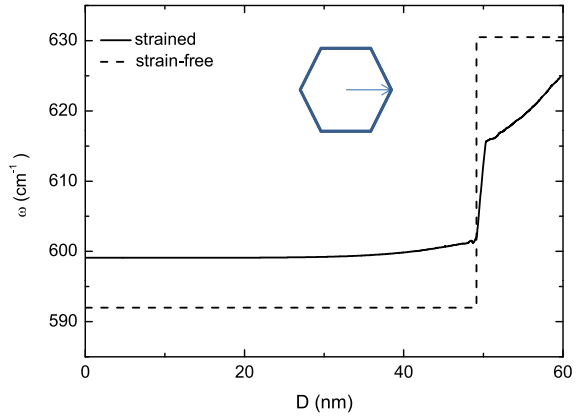

Figure 7. Calculated frequency of the A_1(LO) phonon along the diameter of a core–shell NW with (solid line) and without (dashed line) the inclusion of strain corrections. The characteristics of the core–shell NW are $C_{Ga}^{core} = 4\%$, $R_c = 50$ nm, $C_{Ga}^{shell} = 30\%$ and $t = 10$ nm.

present both in the Ga-richer NW shell and the In-rich core. In the following, the effects of composition and strain fields in the phonon frequencies of core–shell $In_xGa_{1-x}N$ NWs are studied theoretically.

As a first step, the strain distribution induced in wurtzite core–shell NWs by the mismatch between the core and the shell lattice constants is calculated. The model equations to be solved are set out within the framework of the continuum elasticity theory by incorporating the lattice mismatch strain as an initial strain within the core region, and obtaining the resulting strain distribution by the Eshelby inclusion method [36]. Direct simulation of the fully three-dimensional problem is quite time consuming computationally. However, if the wire length is much larger than its width, an approximate two-dimensional solution is possible, which will be very accurate in the NW section far from the ends. This so-called *generalized plane strain solution* depends only on the planar coordinates of the transverse cross-section of the NW (y_1, y_2), and exhibits only four strain components: ε_{11}, ε_{22}, ε_{12}, and ε_{33} [37]. The two-dimensional strain distribution for a core–shell NW of hexagonal section is finally calculated by the finite element method with the COMSOL MULTIPHYSICS software [38]. The lattice parameters and elastic constants for the alloys are obtained by applying Vegard's law to those of the binary materials [39]. The strain-induced frequency shift for a phonon λ is given by $\Delta\omega_\lambda = a_\lambda(\varepsilon_{11} + \varepsilon_{22}) + b_\lambda\varepsilon_{33}$, where a_λ and b_λ are the phonon deformation potentials [40].

The frequencies of the A_1(LO) phonon for the core and the shell alloys with and without taking into account the strain fields in the NW are shown in figure 7 along the NW radius. The parameters of the theoretical model are set according to the results obtained by XRF and HRTEM–EDX and are summarized in table 2: $t = 10$ nm, $R_c = 50$ nm, $C_{Ga}^{core} = 4\%$, and $C_{Ga}^{shell} = 30\%$. For these conditions, the NW core is mostly compressed and the shell presents a tensile strain. Such strain fields cause a nearly constant 7 cm^{-1} phonon blue-shift in the core region and a variation between -15 and -5 cm^{-1} for the shell of the NW. The strain-corrected theoretical predictions compare very well with the two contributions, centered at 597 and 625 cm^{-1}, of the quasi-LO Raman band observed in figure 2(b) for a 785 nm excitation wavelength. Since this laser line is far from the bandgap of 4% and 30% Ga-rich alloys, the intensity of the peaks should be proportional to excited volume. Therefore the two peaks can be attributed to the In-rich core and to the Ga-richer $In_xGa_{1-x}N$ thinner shell, respectively. Decreasing the excitation wavelength below 647 nm leads to the third spectral component in the range of 650–680 cm^{-1} which corresponds to regions with 50–60% Ga content with no strain correction. Such a high Ga concentration could only correspond to the Ga-richest NW base and is consistent with the sharp peak in the HRTEM–EDX axial line-scan of figure 5(c). This shows how the selectivity of RRS does not rely on its spatial resolution, as the laser spot exceeds by far the NW dimensions, but on the spectral resolution of the resonant scattering. Thus tuning the energy of the excitation to match resonant conditions, RRS provides information from very small regions which are hard to probe by other methods.

The results from the three complementary techniques are consistent with the existence of a core–shell structure and a decrease in the shell thickness from the base to the top in each $In_xGa_{1-x}N$ NW. Both trends are common to almost all the samples investigated, independently of the growth conditions (sample G869 has a shell of nearly constant thickness). The average Ga compositions obtained from XRF and HRTEM–EDX in the core and shell regions at a central cross-section are summarized in table 3. All the investigated NWs present values for C_{Ga}^{core} much lower than the Ga supply. Alloy concentrations comparable to c_{Ga} have been found in the NW thin shells wrapping the In-rich cores. The comparison of samples G682 and G692 shows how the growth temperature, despite being critical for the NW size and density, has an imperceptible effect on the alloy distribution.

The findings of this study can throw light on the interplay between the main mechanisms intervening in the catalyst-free MBE growth of $In_xGa_{1-x}N$ NWs: direct impingement, diffusion and desorption for both In and Ga atoms. While the ratio of direct impingement on the top and lateral NW surfaces is determined by the geometry of the MBE chamber only [41],

Table 3. Ga contents, C_{Ga}^{core} and C_{Ga}^{shell}, and core and shell thicknesses, R_c and t, deduced from the fitting of HRTEM–EDX and XRF experimental line-scans (left/right, respectively) for single NWs from the different samples. The results correspond to the cross-section at the central height C of the NWs. Values for t are obtained from the fitting of the HRTEM–EDX line-scans only. The reduced dimensions of NWs labeled G710B were beyond the spatial resolution of XRF, thus the results presented correspond to the average Ga content of the core and shell regions.

Sample	C_{Ga}^{core} (%)	C_{Ga}^{shell} (%)	R_c (nm)	t (nm)
G869	0/2	18/4	80/80	7
G682	2/10	35/25	28/30	4
G692	1/4	35/20	50/70	8
G710A	4/17	35/24	100/80	17
G710B	0/28	40/28	14/20	4

sticking and diffusion coefficients on different crystal planes are very sensitive to the growth temperature [42]. The substrate temperatures of the present NWs are far below 620 °C, which sets the lowest limit for GaN diffusion-induced self-organized NW growth on Si. Therefore Ga atoms should have a very limited diffusion on the substrate and on all facets of the NWs during the growth process, whereas notable diffusion of In atoms can be assumed. Then, the vertical growth of the NWs proceeds with the In and Ga atoms from direct impingement on the top surface and In atoms that diffuse to the top of the NW. For cell ports mounted at 30° with respect to the normal direction, the average metal flux on the top surface is five to six times higher than that on the sidewalls [41]. However, tables 2 and 3 report a significant difference between the relative Ga content measured in most of the NW volume and the metal supply, which can only be interpreted as a signature of the dominant role of In diffusion in the NW growth. Differences in the diffusion and desorption of Ga and In atoms can also explain the spontaneous formation of the Ga-richer shell. After impinging on the sidewalls, In atoms can either diffuse towards the top of the NW or get desorbed, whereas Ga atoms are expected to incorporate there, as their diffusion and desorption are highly suppressed. Therefore, the NWs should grow laterally at a much lower growth rate due to the accumulation of Ga atoms.

5. Conclusions

In conclusion, x-ray fluorescence, energy-dispersive x-ray spectroscopy and resonant Raman scattering have been employed to study In-rich $In_xGa_{1-x}N$ NWs grown by MBE. The combination of the three techniques results in a reliable picture of the alloy composition within each NW and reveals the existence of a core–shell alloy distribution. Following a careful analysis of the spatial resolution and chemical sensitivity of each technique, the alloy concentration, the dimensions and the strain components of the core and shell regions within single NWs have been provided. The spontaneous formation of a core–shell structure supports the idea of NW growth being dominated by the diffusion of In and suggests new strategies for achieving high quality non-polar heterostructures.

Acknowledgments

This work has been supported by the European Union through the grant agreement no. 265073-NANOWIRING of the Seventh Framework Program and by project MAT2012-33483 and GICSERV NGG-121 of the Spanish Ministry of Finances and Competitiveness.

References

[1] Yoshizawa M, Kikuchi A, Mori M, Fujita N and Kishino K 1997 *Japan. J. Appl. Phys.* **36** L459
[2] Calleja E, Sánchez-García M A, Sánchez F J, Calle F, Naranjo F B, Muñoz E, Jahn U and Ploog K 2000 *Phys. Rev.* B **62** 16826
[3] Stoica T, Meijers R J, Calarco R, Richter T, Sutter E and Luth H 2006 *Nano Lett.* **6** 1541
[4] Landre O, Fellmann V, Jaffrennou P, Bougerol C, Renevier H, Cros A and Daudin B 2010 *Appl. Phys. Lett.* **96** 061912
[5] Kuykendall K, Ulrich P, Aloni S and Yang P 2007 *Nature Mater.* **6** 951
[6] Xiang H J, Wei S H, Da Silva J L F and Li J 2008 *Phys. Rev.* B **78** 193301
[7] Ho I H and Stringfellow G B 1996 *Appl. Phys. Lett.* **69** 2701
[8] Qian F, Li Y, Gradečak S, Park H G, Dong Y J, Ding Y, Wang Z L and Lieber C M 2008 *Nature Mater.* **7** 701
[9] Vajpeyi A P, Ajagunna A O, Tsagaraki K, Androulidaki M and Georgakilas A 2009 *Nanotechnology* **20** 325605
[10] Kahagias T 2010 *Physica* E **42** 2197
[11] Tabata T, Paek J, Honda Y, Yamaguchi M and Amano H 2012 *Phys. Status Solidi* c **9** 646
[12] Limbach F *et al* 2011 *J. Appl. Phys.* **109** 014309
[13] Tourbot G, Bougerol C, Grenier A, Den Hertog M, Sam-Giao D, Cooper D, Gilet P, Gayral B and Daudin B 2011 *Nanotechnology* **22** 075601
[14] Goodman K D, Protasenko V V, Verma J, Kosel T H, Xing H G and Jena D 2011 *J. Appl. Phys.* **109** 084336
[15] Albert S, Bengoechea-Encabo A, Lefebvre P, Sanchez-Garcia M A, Calleja E, Jahn U and Trampert A 2011 *Appl. Phys. Lett.* **99** 131108
[16] Armitage R and Tsubaki K 2010 *Nanotechnology* **21** 195202
[17] Bavencove A L, Tourbot G, Garcia J, Désières Y, Gilet P, Levy F, André B, Gayral B, Daudin B and Le Si Dang D 2011 *Nanotechnology* **22** 345705
[18] Knelangen M, Hanke M, Luna E, Schrottke L, Brandt O and Trampert A 2011 *Nanotechnology* **22** 365703
[19] Tourbot G, Bougerol C, Glas F, Zagonel L F, Mahfoud Z, Meuret S, Gilet P, Kociak M, Gayral B and Daudin B 2012 *Nanotechnology* **23** 135703
[20] Bardoux R, Funato M, Kaneta A, Kawakami Y, Kikuchi A and Kishino K 2013 *Opt. Mater. Express* **3** 47
[21] Martínez-Criado G *et al* 2012 *J. Synchrotron Radiat.* **19** 10
[22] Solé V A, Papillon E, Cotte M, Walter Ph and Susini J 2007 *Spectrochim. Acta* B **62** 1
[23] Loudon R 1964 *Adv. Phys.* **13** 423
[24] Harima H 2002 *J. Phys.: Condens. Matter* **14** R967
[25] Segura-Ruiz J, Garro N, Cantarero A, Denker C, Malindretos J and Rizzi A 2009 *Phys. Rev.* B **79** 115305
[26] Schäfer-Nolte E O, Stoica T, Gotschke T, Limbach F, Sutter E, Sutter P, Grützmacher D and Calarco R 2010 *Nanotechnology* **21** 315702
[27] Hernández S, Cuscó R, Pastor D, Artús L, O'Donnell K P, Martin R W, Watson I M, Nanishi Y and Calleja E 2005 *J. Appl. Phys.* **98** 013511
[28] Segura-Ruiz J *et al* 2011 *Phys. Status Solidi RRL* **5** 95

[29] Walukiewicz W, Ager J W, Yu K M, Liliental-Weber Z, Wu J, Li S X, Jones R E and Denliger J D 2006 *J. Phys. D: Appl. Phys.* **39** R83
[30] Segura-Ruiz J, Martínez-Criado G, Chu M H, Geburt S and Ronning C 2011 *Nano Lett.* **11** 5322
[31] Van Grieken R E and Markowicz A A 2002 *(Practical Spectroscopy Series* vol 29) (New York: Marcel Dekker)
[32] Smeeton T M, Kappers M J, Barnard J S, Vickers M E and Humphreys C J 2003 *Appl. Phys. Lett.* **83** 5419
[33] Lorimer G W 1987 *Mineral. Mag.* **51** 49
[34] Bell C D, Wu Y, Barrelet C J, Gradeăk S, Xiang J, Timko B P and Lieber C M 2004 *Microsc. Res. Tech.* **64** 373
[35] Gómez-Gómez M, Garro N, Segura-Ruiz J, Martinez-Criado G, Chu M H, Cantarero A, Denker C, Malindretros J and Rizzi A 2013 *Phys. Status Solidi RRL* **10** 864
[36] Eshelby J D 1957 *Proc. R. Soc.* A **241** 376
[37] Blazquez A, Mantic V and Paris F 2006 *Eng. Anal. Bound. Elem.* **30** 489
[38] For detailed documentation, see comsol website www.comsol.com/
[39] Morales F M, Gonzalez D, Lozano J G, Garcia R, Hauguth-Frank S, Lebedev V, Cimalla V and Ambacher O 2009 *Acta Mater.* **57** 5681
[40] Demangeot F, Frandon J, Renucci M A, Briot O, Gil B and Aulombard R L 1996 *Solid State Commun.* **207** 100
Wright A F 1997 *J. Appl. Phys.* **82** 2833
[41] Foxon C T, Novikov S V, Hall J L, Campion R P, Griffiths I and Khongphetsak S 2009 *J. Cryst. Growth* **311** 3423
[42] Lymperakis L and Neugebauer J 2009 *Phys. Rev.* B **79** 241308(R)